

A *Chandra* STUDY OF THE GALACTIC GLOBULAR CLUSTER OMEGA CENTAURIDARYL HAGGARD<sup>1,2</sup>, ADRIENNE M. COOL<sup>3</sup>, AND MELVYN B. DAVIES<sup>4</sup>*Accepted for publication in The Astrophysical Journal*

## ABSTRACT

We analyze a  $\sim 70$  ksec *Chandra* ACIS-I exposure of the globular cluster  $\omega$  Cen (NGC 5139). The  $\sim 17' \times 17'$  field of view fully encompasses three core radii and almost twice the half-mass radius. We detect 180 sources to a limiting flux of  $\sim 4.3 \times 10^{-16}$  erg cm<sup>-2</sup> s<sup>-1</sup> ( $L_x = 1.2 \times 10^{30}$  erg sec<sup>-1</sup> at 4.9 kpc). After accounting for the number of active galactic nuclei and possible foreground stars, we estimate that 45-70 of the sources are cluster members. Four of the X-ray sources have previously been identified as compact accreting binaries in the cluster—three cataclysmic variables (CVs) and one quiescent neutron star. Correlating the *Chandra* positions with known variable stars yields eight matches, of which five are probable cluster members that are likely to be binary stars with active coronae. Extrapolating these optical identifications to the remaining unidentified X-ray source population, we estimate that 20-35 of the sources are CVs and a similar number are active binaries. This likely represents most of the CVs in the cluster, but only a small fraction of all the active binaries. We place a  $2\sigma$  upper limit of  $L_x < 3 \times 10^{30}$  erg sec<sup>-1</sup> on the integrated luminosity of any additional faint, unresolved population of sources in the core. We explore the significance of these findings in the context of primordial vs. dynamical channels for CV formation. The number of CVs per unit mass in  $\omega$  Cen is at least 2-3 times lower than in the field, suggesting that primordial binaries that would otherwise lead to CVs are being destroyed in the cluster environment.

*Subject headings:* binaries: close — globular clusters: individual ( $\omega$  Centauri) — novae, cataclysmic variables — stars: neutron — X-rays: binaries

## 1. INTRODUCTION

Binary stars are key players in globular cluster dynamics. Increasingly sophisticated numerical modeling in recent years has revealed a complex interplay between stellar dynamics and stellar evolution in these clusters (*e.g.*, Ivanova et al. 2006; Fregeau 2008; Fregeau et al. 2003). A critical component of all such models are binary stars—both the primordial population and any population subsequently created or modified through stellar interactions. Observations that can constrain and characterize binary populations are thus essential to understanding globular cluster evolution.

Observations at X-ray wavelengths have become a prime tool in the study of binary star populations in globular clusters. The *Chandra X-ray Observatory's* high spatial resolution and resulting sensitivity to point sources makes it possible to obtain nearly complete samples of compact accreting binaries in nearby globular clusters and brings within reach new classes of fainter binaries. The ability to pinpoint the location of the sources to  $< 1''$  also means that the stars responsible for the emission may be recovered at other wavelengths even in the crowded fields of globular clusters.

$\omega$  Centauri is of particular interest for multiple reasons. With an estimated  $4 \times 10^6 M_\odot$  (Meylan 2002), it is the most massive globular cluster in the Milky Way. Its stellar populations reveal a complexity not typical of globular clusters, which has led to the suggestion that it may

instead be the remnant of a dwarf galaxy that merged with the Milky Way (see Piotto et al. 2005; Bedin et al. 2004; Gratton, Sneden, & Carretta 2004, and references therein). At 4.9 kpc the cluster is relatively nearby, making it possible to detect low-luminosity X-ray sources in modest exposure times with *Chandra*. Owing to its large core ( $r_c = 155'' = 3.7$  pc<sup>5</sup>; Trager, King & Djorgovski 1995),  $\omega$  Cen has a relatively high rate of stellar interactions despite a modest central density of  $\rho_0 \sim 3 \times 10^3 M_\odot$  pc<sup>-3</sup> (Pryor & Meylan 1993). Well-described by a King model (Meylan 2002), it has been the subject of multiple studies aimed at predicting its accreting binary population (Verbunt & Meylan 1988; Davies & Benz 1995; Di Stefano & Rappaport 1994).

The *Einstein* IPC survey of globular clusters was the first study to reveal a population of X-ray sources toward  $\omega$  Cen (Hertz & Grindlay 1983). Of the five sources found in the *Einstein*/IPC field, the three farthest from the cluster center (all located at more than  $4 r_c$ ) were later shown or suggested to be foreground stars (Cool et al. 1995; Margon & Bolte 1987). With ROSAT-HRI, the central *Einstein* IPC source (“C”) was resolved into three sources in the cluster core (Verbunt & Johnston 2000). All three appear to be cataclysmic variables (CVs; see §5). The position of the fifth Hertz & Grindlay (1983) *Einstein* source (“B”), at  $1.7 r_c$ , is consistent with that of the transient neutron star in quiescence identified by

<sup>1</sup> Dept. of Astronomy, University of Washington, Box 351580, Seattle, WA 98195; dhaggard@astro.washington.edu

<sup>2</sup> NASA Harriett G. Jenkins Fellow

<sup>3</sup> Dept. of Physics and Astronomy, San Francisco State University, 1600 Holloway Ave., San Francisco, CA 94132; cool@sfsu.edu

<sup>4</sup> Lund Observatory, Box 43, SE-221 00, Lund, Sweden; mbd@astro.lu.se

<sup>5</sup> This value of the core radius is larger than that found by van Leeuwen et al. (2000) which is quoted in the 2003 version of the Harris (1996) catalog. We adopt it as it is in good agreement with recent measurements by both McLaughlin & Meylan (2003) and J. Anderson (private communication); the latter is based on star counts from HST/ACS imaging of the central  $11' \times 11'$  of the cluster.

Rutledge et al. (2002). With ROSAT, the number of X-ray sources known toward  $\omega$  Cen grew to 21, 7 of which lie within  $3 r_c$  (Johnston, Verbunt & Hasinger 1994; Verbunt & Johnston 2000). Most recently, Gendre et al. (2003) detected 146 sources toward  $\omega$  Cen,  $\sim 70$  of which lie within  $3 r_c$ .

Here we present results of a  $\sim 70$  ksec observation of  $\omega$  Cen with *Chandra*'s Advanced CCD Imaging Spectrometer (ACIS). Preliminary results were reported by Cool, Haggard & Carlin (2002) and Haggard et al. (2002a). An analysis of  $\sim 40$  of the brightest sources in these data was presented by Rutledge et al. (2002) in their X-ray spectroscopic search for transient neutron stars in quiescence. We describe the *Chandra* observations in §2, and our source detection and analysis methods in §3. In §4 we estimate the number of active galactic nuclei (AGN) present in the field in order to determine how many of the observed sources are likely to be cluster members. In §5 we present results of our search for optical counterparts to the *Chandra* sources among existing catalogs of variable stars in and toward  $\omega$  Cen. We also summarize the results of our previous efforts to identify counterparts of some of these sources using Hubble Space Telescope (HST). Complete results of our search for optical counterparts using HST's ACS/WFC will be reported in a forthcoming paper (Cool et al. 2009). We explore the nature of the X-ray source population in  $\omega$  Cen in §6 and summarize our results in §7.

## 2. X-RAY OBSERVATIONS

We obtained two exposures of  $\omega$  Cen using the imaging array of the Advanced CCD Imaging Spectrometer (ACIS-I) on January 24–25, 2000 in “very faint” mode. The total exposure time was 72.4 ksec. The camera was oriented so as to insure that the three previously known core sources would not land in the gaps between the four ACIS-I chips.

Beginning with the level-one events files, we used the additional information telemetered in very faint mode (a  $5 \times 5$  pixel event island instead of the faint mode's  $3 \times 3$  island) to improve the filtering out of particle background events<sup>6</sup>. This procedure significantly reduced the background levels in both exposures. Enhanced charge transfer inefficiency (CTI) in the ACIS-I front-illuminated chips, due to damage from the Earth's radiation belts, was also known to make the gain, event grade, and energy resolution row-dependent. To mitigate these effects we applied the CTI corrector developed by Townsley et al. (2000). The CTI corrector also recognized cosmic ray events and flagged them for removal. Next, we filtered out bad pixels and cosmic rays and applied the standard event grade filtering, keeping only events with ASCA grades 0, 2, 3, 4, and 6. We also removed pixel randomization since the exposure was long enough that the telescope dither served the same purpose. After selecting only good time intervals, the combined effective exposure time of the two observations was 68.6 ksec. The final step was to re-project the two exposures to a single R.A. and Dec., and merge them into one image for purposes of source detection. This was accomplished using the

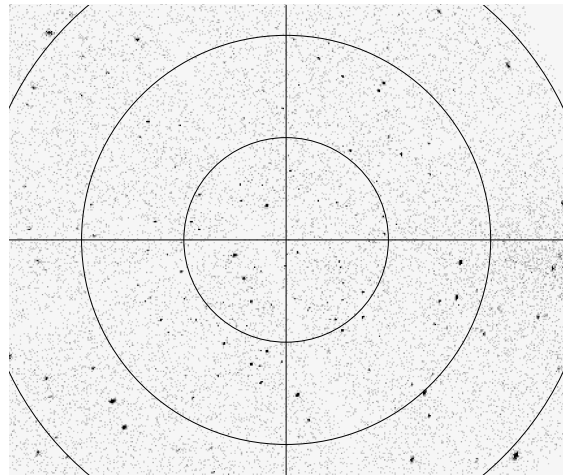


FIG. 1.— Merged,  $\sim 70$  ksec *Chandra* ACIS-I image of the core of  $\omega$  Cen. The large circles represent 1, 2, and 3 times the core radius; cross-hairs mark the cluster center. North is up and east is to the left.

*merge\_all* script which also created an associated merged exposure map. These procedures (with the exception of the CTI corrector) were all carried out using the CIAO software tools.

The background level in the 0.5–4.5 keV energy range is  $\sim 0.034$  counts/sq.arcsec near the center of the image and drops about 13% at  $\sim 10'$  off-axis due to vignetting. A search for evidence of time intervals containing elevated background levels (“flares”) yielded none. We constructed the exposure map for the combined image to account for the vignetting and the reduced effective exposure time in the chip gaps. The overall background levels are slightly lower than typical on-orbit background levels, perhaps owing to the extra event filtering made possible by use of the very faint mode.

In Fig. 1 we show the combined image of the central portion of the ACIS-I field. Numerous faint point sources can be seen, along with a smaller number of bright sources. Careful examination also reveals the broadening and distortion of the point-spread function (PSF) with increasing off-axis angle.

## 3. X-RAY SOURCE DETECTION AND ANALYSIS

After experimenting with source detection algorithms and energy ranges, we settled on using the wavelet-based algorithm implemented in CIAO's *wavdetect*. We applied it to the subset of events with energies in the range 0.5–4.5 keV in the four ACIS-I chips. The chip S-2 in the ACIS-S array was also active during both observations, but we did not analyze data from this chip since the PSF is very broadened. Removing events with energies above 4.5 keV reduced the background level noticeably. This energy range was also chosen for ease of comparison to *Chandra* studies of other globular clusters.

We adopted a source significance threshold of  $10^{-6}$ , which gives  $\sim 1$  false detection per  $10^6$  pixels (Freeman et al. 2002), and wavelet (spatial) scales of 1 to 16 in intervals of  $\sqrt{2}$ . Given the low background level in our chosen energy range, an on-axis source with just 4 counts in a  $1''$  radius ( $> 90\%$  encircled energy) has a Poisson probability  $\sim 5 \times 10^{-6}$  and is likely to be real. Off axis, as the PSF broadens, reliable detections require increasingly large numbers of counts.

<sup>6</sup> See Alexey Vikhlinin's summary at <http://hea-www.harvard.edu/~alexey/vf.bg/vfbg.html> and <http://cxc.harvard.edu/ciao/threads/acisclean/vf/>.

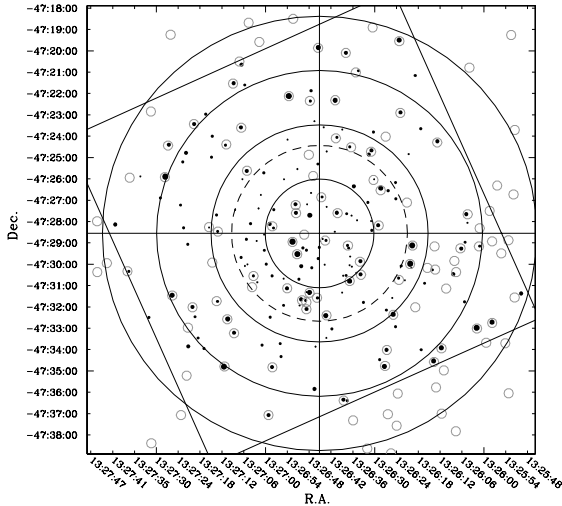


FIG. 2.— The 180 *Chandra* X-ray sources (filled circles) in the field of the ACIS-I camera (large square). The area of each circle is proportional to X-ray flux of the source it represents. Open grey symbols indicate sources detected by XMM (Gendre et al. 2003). Large solid circles represent 1, 2, 3, and 4 core radii; the large dashed circle represents the cluster half-mass radius. North is up and east is to the left.

The above combination of parameters yielded 171 sources in the inner  $2048 \times 2048$  pixels (unbinned; 1 pix =  $0''.492$ ) and an additional 9 sources in a binned ( $2 \times 2$ ) version of the image, which included the corners of the field excluded in the unbinned image. The resulting list of 180 sources was similar to source lists we formulated using other methods, including one created with *celldetect*, and those generated from a combination of Poisson analysis and visual examination. Fig. 2 shows the 180 X-ray sources in the full field of the ACIS-I detector together with circles indicating 1, 2, 3, and 4 core radii as well as the half-mass radius (dashed circle).

For ease of locating sources in the image, we have named each according to its radial offset from the cluster center and the quadrant in which it falls (see Fig. 3). The first character in the ID represents the radial offset in arcminutes (rounded to the nearest arcminute, except for sources less than  $0'.5$  from the center, which are also assigned a first digit of “1”). The second character (1–4) represents the quadrant in which the source falls (counterclockwise from the northwest quadrant “1”). The last character is a letter (a–l), in order of azimuthal position (working counterclockwise) within a given annulus and quadrant. These designations appear in Table 1, column 1. In column 2 we list the official CXC designation of the source<sup>7</sup>, in J2000 coordinates; column 3 gives the radial offset from the cluster center in units of core radii. Uncertainties in these positions will be a combination of the uncertainty in the absolute pointing of the spacecraft ( $\sim 0.6''$ ) and the uncertainty in centroiding the counts associated with each source. The latter contribution has been estimated by Feigelson et al. (2002) to be  $\sim 0''.25$  for off-axis angles of  $\theta \lesssim 1'$ ,  $0''.5$  at  $\theta \sim 4'.5$ , and  $\sim 2'' - 5''$  toward the edge of the field ( $\theta \sim 8' - 12'$ ).

We determined source counts using 95% encircled energy radii as determined from model point-spread functions, derived using the CIAO tool *mkpsf* at an interme-

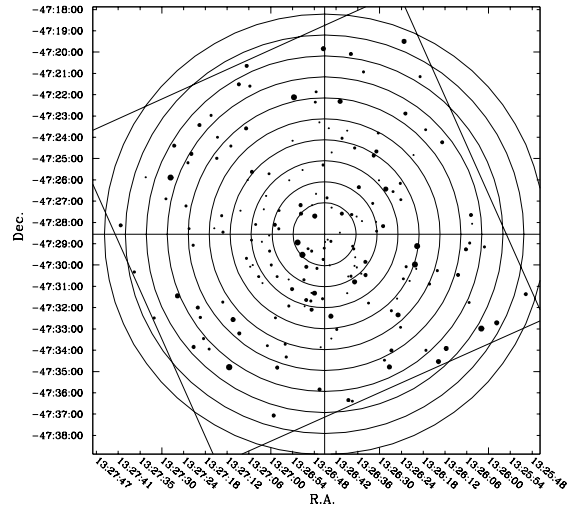


FIG. 3.— Axes and symbols as in Fig. 2, here with  $1'$  annuli marked; the first annulus goes from the cluster center to  $1'.5$ , the second from  $1'.5$  to  $2'.5$ , the third from  $2'.5$  to  $3'.5$ , etc., out to  $10'.5$ . These annuli are adopted for the source designations described in §3 and found in the first column of Table 1.

mediate energy of  $\sim 1.5$  keV (the PSF shape being somewhat energy dependent). Counts were extracted in three bands: “soft” (0.5–1.5 keV), “medium” (0.5–4.5 keV), and “hard” (1.5–6.0 keV). We determined the background to subtract from each source by dividing the image into  $1'$ -wide annuli centered on the aim point in chip 3 (the innermost “annulus” being a circle of radius  $1.5'$ ). Background values adopted for sources in a given annulus were averages determined from several source-free regions within that annulus, after verifying that the background levels were azimuthally symmetric. For twelve sources (11b, 12b, 13e, 22c, 32c, 41b, 41c, 84a, 84b, 84c, 93a, and 93b) that fell in the chip gaps or near the outer edge of a chip, background regions were chosen specifically to reflect these conditions. Local background determinations were also made for a small number of sources to the west of the cluster center that lie on or near a large diffuse X-ray source  $\sim 7'$  west of the cluster center (see below). Following background subtraction, we applied aperture corrections and also corrected for reduced effective exposure times off-axis and in the chip gaps using the exposure map.

Raw and corrected source counts for the medium, soft, and hard bands appear in columns 4–6 of Table 1, respectively. The hardness ratio, defined as the number of soft counts divided by the number of hard counts, is given in column 8. In column 9 we list the X-ray flux derived from the medium counts values in column 4. We used WebPIMMS to estimate that one ACIS-I count per second is equal to an unabsorbed flux of  $7.3 \times 10^{-12}$  erg  $\text{cm}^{-2}$   $\text{s}^{-1}$  in the 0.5 – 2.5 keV *ROSAT* band, based on a 1 keV thermal bremsstrahlung spectrum, with an assumed hydrogen column of  $N_H = 9 \times 10^{20}$   $\text{cm}^{-2}$ . All but two sources in the final *wavdetect* list have at least 4 counts. This represents a detection limit of  $f_x \sim 4.3 \times 10^{-16}$  erg  $\text{cm}^{-2}$   $\text{s}^{-1}$  ( $L_x \sim 1.2 \times 10^{30}$  erg  $\text{sec}^{-1}$  at a distance of 4.9 kpc) — about an order of magnitude fainter than the XMM detection limit (Gendre et al. 2003).

Of the 180 sources we report, 113 are new (see column 10 of Table 1). The other 67 were all detected with XMM (Gendre et al. 2003) with the ex-

<sup>7</sup> See Dictionary of Nomenclature of Celestial Objects at <http://vizier.u-strasbg.fr/viz-bin/Dic>.

ception of 12a, which was detected with ROSAT-HRI but not with XMM. Source 12a, which has been identified optically as a CV (see §5), is the third brightest source in the core in the present observations; thus it must be highly variable. Ten of the XMM sources had previously been detected with ROSAT-HRI and/or ROSAT-PSPC (Verbunt & Johnston 2000; Johnston, Verbunt & Hasinger 1994). Thirty-six of the brightest *Chandra* sources in the ACIS-I field were also previously reported by Rutledge et al. (2002) in their X-ray spectroscopic search for transient neutron stars in quiescence. Interestingly, 24 of the XMM sources within our field of view have no *Chandra* counterpart (see Fig. 2). Clearly there is a high degree of variability, such that a complete census requires repeated observations at multiple epochs.

Finally, we confirm the presence of an extended source of emission west of the cluster center. It appears roughly oval in shape, centered at (R.A., Dec.) = (13:26:08.2, -47:29:06) with a  $\sim 2.0$  major axis running roughly east-west and a minor axis of  $\sim 1.6$ . Signs of this diffuse emission were first reported by Hartwick, Grindlay, & Cowley (1982) based on *Einstein* IPC imaging. Though not seen with ROSAT (Johnston, Verbunt & Hasinger 1994), the extended emission is seen clearly both with *Chandra* with XMM (Gendre et al. 2003). A detailed analysis of the *Chandra* data by Okada et al. (2007) concludes that the emission probably does not originate in the cluster, but instead arises from a poor cluster of galaxies at  $z = 0.1 - 0.2$ . Eight of the point sources in Table 1 overlap the extended emission region (44e, 64d, 71a, 71b, 74d, 74e, 74f, and 84f), four of which are also XMM sources. A few additional XMM sources in the region (see Fig. 2) may be spurious, as noted by Gendre et al. (2003). Given the higher spatial resolution of *Chandra* and our use of local background levels in measuring sources in this region, we do not expect any significant number of spurious detections among the *Chandra* sources. Indeed, we find no significant increase in source numbers in this region as compared to other regions of similar size at comparable off-axis angles in the ACIS-I field.

#### 4. X-RAY SOURCE MEMBERSHIP

Given the field of view and sensitivity of *Chandra*, and the relatively long exposure we have obtained of  $\omega$  Cen, we expect a significant fraction of the sources in the ACIS-I field to be active galactic nuclei. To investigate this question, we begin by plotting the distribution of *Chandra* sources as a function of radius in the ACIS-I field (see Fig. 4). For each source, the log of the background-corrected medium-band counts is plotted against the square of the angular distance from the aimpoint, which is  $\sim 20''$  from the cluster center. In this representation, a spatially uniform distribution of sources would appear evenly spread, out to the radius at which the ACIS-I coverage begins to be incomplete ( $\sim 8'$ , or  $\sim 60$  square arcminutes; see Fig. 3). The gradual loss of sensitivity with increasing distance from the aimpoint, due to broadening of the PSF, complicates this analysis and is readily apparent in Fig. 4; fainter sources can be detected near the aimpoint than far off-axis. Nevertheless, a careful inspection of this distribution reveals a clear enhancement in the numbers of X-ray sources in the central regions, suggestive of a substantial population of

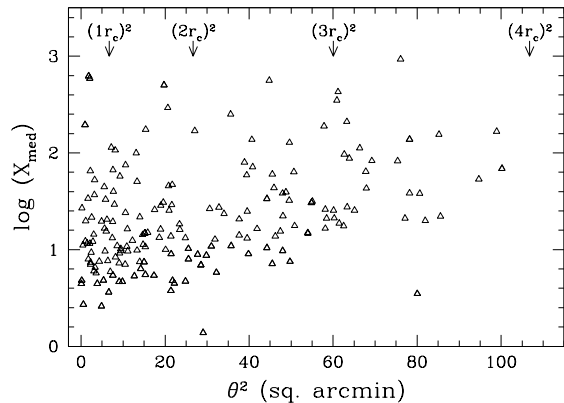


FIG. 4.— *Chandra* source fluxes as a function of the square of the angular distance from the aimpoint. A spatially uniform distribution of sources would appear evenly spread out to the radius at which the ACIS-I coverage begins to be incomplete (see §4). Note the gradual loss of sensitivity with increasing distance from the aimpoint due to broadening of the PSF; fainter sources can be detected near the aimpoint than far off-axis.

cluster members.

To quantify the number of sources likely to be cluster members, we must first determine how many AGN are expected in the field. To this end, we made use of the *Chandra* Deep Field South (CDFS) results reported by Tozzi et al. (2001) and Giacconi et al. (2001). In order to compare our fluxes to theirs, we remeasured counts for all 180 sources in the CDFS 0.5 – 2.0 keV soft band (Table 1, column 7). For the present estimates, we also adopted their flux conversion factor ( $4.6 \times 10^{-12}$  erg  $s^{-1}$   $cm^{-2}$  per count  $s^{-1}$ ; Tozzi et al. 2001), but multiplied this by 1.16 to account for the higher  $N_H$  column to  $\omega$  Cen vs. the *Chandra* Deep Field–South ( $9 \times 10^{20}$   $cm^{-2}$  vs.  $8 \times 10^{19}$   $cm^{-2}$ ). This correction factor was determined assuming a power-law spectrum with  $\Gamma=1.4$ . We use this conversion factor together with Eq.(1) of Tozzi et al. (2001) to predict the number of AGN present above any given count level in the cluster core and in three concentric annuli around the core (1-2  $r_c$ , 2-3  $r_c$ , and 3-4  $r_c$ ). The inner three regions are fully encompassed within the ACIS-I field of view; the outermost region we estimate to be 63% covered (see Fig. 2).

In Fig. 5 we show the cumulative number of observed sources (thin solid line) in each of the four regions as a function of counts in the CDFS soft band together with the number of AGN predicted (long-dash line). Two different uncertainty ranges on the AGN predictions are shown: (1) values derived from Tozzi et al. (2001) Equation 1 (short-dash lines); and (2)  $\pm$  the square root of the predicted number of sources, i.e.  $\pm 1$  sigma assuming Gaussian statistics (dotted lines). The difference between the observed numbers and predicted numbers are shown as thick solid lines. Here we can see that as fainter fluxes are sampled, the number of observed sources and number of predicted AGN both grow. As the detection limit is approached, the number of observed sources begins to flatten out, while the predicted AGN numbers (which do not take our ACIS-I detection limit into account) continue to rise. The difference (dark solid line) reaches a peak in the vicinity of the detection limit. For each region, we take this peak value to be the number of sources that cannot be attributed to AGN. The uncertainty on this number is due to the uncertainty in the

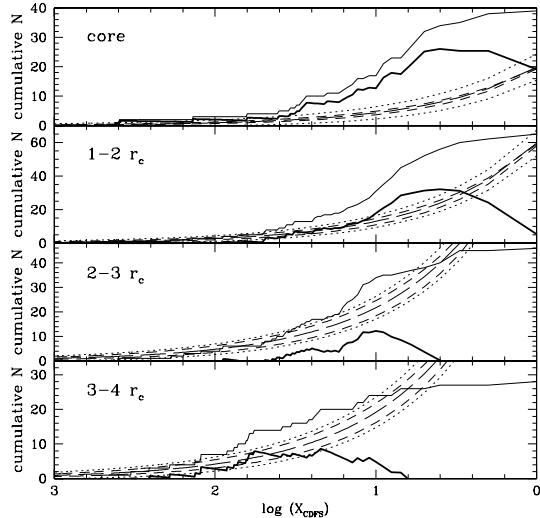


FIG. 5.— Cumulative number of observed sources in the ACIS-I field as a function of counts in the 0.5-2.0 keV band used in the Tozzi et al. (2001) analysis of the *Chandra* Deep Field South (thin solid lines), with the ACIS-I field divided into four regions. Numbers of AGN predicted for this band using Eq.(1) of Tozzi et al. (2001) are shown as long-dash lines, with uncertainties from Eq (1) as short-dash lines. Dotted lines represent Gaussian statistical uncertainties on the Tozzi et al. (2001) predictions. Thick lines show the number of sources not attributable to AGN (i.e. the difference between the thin solid line and the long-dash lines).

number of AGN in the region, which can be judged from the spread between the dotted lines at the location of the peak difference.

In all regions of  $\omega$  Cen covered by ACIS-I, the number of observed sources exceeds the number of AGN predicted. In the core and inner-most annulus, the excess is very significant ( $>6\sigma$ ):  $26 \pm 3$  sources in the core, and  $32 \pm 5$  sources in the 1-2  $r_c$  annulus. In the core, an excess is present over the entire range of observed fluxes. Farther out in the cluster the numbers are smaller and more uncertain:  $12 \pm 5$  and  $8 \pm 3$  in the 2-3  $r_c$  and 3-4  $r_c$  annuli, respectively. We note that these results are similar to results obtained using a different approach in which we divided the field into  $1'$ -wide annuli, took the 3rd, 5th, or 7th-faintest source as a measure of the flux limit in each annulus, and subtracted off the number of AGN predicted to that limit. Hence, the results above are not sensitive to the somewhat variable sensitivity within the  $1 r_c$ -wide annuli adopted for Fig. 5.

Some fraction of the remaining X-ray sources could be foreground stars. Indeed, we have already identified several as such (see §5 and Table 2). Given that five of the  $\sim 8$  sources in the 3-4  $r_c$  annulus that are not attributed to AGN are stellar, it seems likely that few, if any, of the sources observed at  $>3 r_c$  are cluster members. Among the  $\sim 70$  sources inside  $3 r_c$  that are not attributed to AGN, we can place an upper limit on the number of foreground sources as follows. First, we note that of the  $\sim 12$  sources in the 2-3  $r_c$  annulus that are not AGN, four have been identified optically as probable cluster members (see §5 and Table 2). If we assume that the remaining  $\sim 8$  sources are all foreground stars, then scaling by area, we estimate that  $\sim 5$  foreground stars may be present in the 1-2  $r_c$  annulus and another  $\sim 2$  in the core. If we further account for the fact that somewhat

fainter sources (a factor of  $\sim 1.5 - 2$ ) can be detected in those regions than in the 2-3  $r_c$  annulus, and assume that the number of foreground sources scales as  $f_x^{-1.5}$  (i.e., assuming a uniformly distributed population, where  $f_x$  is the flux limit), then an additional  $\sim 2 - 4$  sources in the core and  $\sim 4 - 9$  sources in the 1-2  $r_c$  annulus could be in the foreground. We thus estimate that up to  $\sim 25$  of the sources inside  $3 r_c$  could be foreground stars; the actual number may be considerably lower.

In summary, the total number of sources inside  $3 r_c$  that are likely to be cluster members is  $\sim 45-70$ , with an additional uncertainty of  $\pm 8$  due to the uncertainty in the number of AGN present. Of these,  $\sim 21-26$  are in the core,  $\sim 20-32$  in the 1-2  $r_c$  annulus, and  $\sim 4-12$  in the 2-3  $r_c$  annulus. Few, if any, of the sources outside  $3 r_c$  are likely to be cluster members.

## 5. OPTICAL IDENTIFICATIONS

To establish which of the X-ray sources toward  $\omega$  Cen are the cluster members, optical identifications are needed. For stars that are relatively bright and/or in the outer regions of the cluster, such identifications may be made using ground-based data. In the central regions of the cluster, where the crowding is severe, we have undertaken searches for counterparts using Hubble Space Telescope (HST). The full results of our ACS/WFC search for optical counterparts to the *Chandra* sources will be reported in a separate paper (Cool et al. 2009). Here we summarize results of that study that have already appeared, results of an earlier WFPC2 study, and our efforts to identify optical counterparts among stars in existing ground-based catalogs.

Using HST, we have identified four of the brightest *Chandra* sources (12a, 13a, 13c, and 44e) as probable compact accreting binaries. Carson, Cool & Grindlay (2000) used HST/WFPC2 to search for optical counterparts of the first three (the brightest sources in the cluster core), using ROSAT-HRI positions. Searching the HRI error circles, they found blue, H $\alpha$ -bright counterparts for two of the sources and identified them as probable cataclysmic variables. The XMM spectra of these two sources further support their identity as CVs (Gendre et al. 2003). We also identified a tentative optical counterpart for the third source on the basis of its H $\alpha$  excess (Carson, Cool & Grindlay 2000). This star has since been shown to be blue in ACS/WFC imaging and is thus also likely to be a CV (Haggard et al. 2002b, 2003). All three stars were subsequently shown to have ACS/WFC coordinates that are very well matched to the *Chandra* coordinates (Haggard et al. 2004). These three stars are named CV1-3 in Tables 1 and 2. The fourth *Chandra* source (44e) was shown by Rutledge et al. (2002) to be a probable transient neutron star in quiescence (qNS) on the basis of its X-ray spectrum and luminosity. Haggard et al. (2004) found a faint blue, H $\alpha$ -bright optical counterpart for this source using ACS/WFC, further supporting this identification. Columns 5 and 6 of Table 2 list the pre-boresite offsets between the optical and X-ray positions for these four sources. Following a boresite correction of  $(\Delta\alpha, \Delta\delta) = (0''.0, 0''.3)$ , all four match to within  $\pm 0''.2$  in both R.A. and Dec. (Table 2, columns 7 and 8), which further secures their identifications.

We have also compared the 180 *Chandra* source positions to two catalogs of variable stars: Kaluzny et al.

(2004) and Weldrake, Sackett & Bridges (2007). Here we initially required that sources match within  $1\text{--}2''$ , depending on their radial position in the cluster, and focused our search on sources in the inner 8 annuli. This produced a set of 9 tentative identifications. We then used these tentative matches to determine a preliminary boresite correction. Following this correction, we recomputed the offsets and applied more stringent matching criteria following Feigelson et al. (2002, see §3). In the inner 4 annuli, we required matches to within  $0''.5$ ; for annuli 5-8 we required matches to within  $1''.0$ . This eliminated 2 of the tentative matches. Recomputing the boresite correction for the remaining 7 sources yields  $(\Delta\alpha, \Delta\delta) = (0''.5, 0''.5)$ . Pre-boresite offsets are listed in columns 5 and 6 of Table 2; offsets that remain after the boresite correction has been applied are listed in columns 7 and 8. That the X-ray and optical coordinates of all 7 sources match to within  $\pm 0''.3$  in both R.A. and Dec. following the boresite correction further secures their identifications. Finally, we expanded our search for matches to the outer annuli, requiring post-boresite matches of  $3''$  and  $4''$  in annuli 9 and 10, respectively. This yielded one additional match in the 9th annulus, for a total of 8 matches to the 271 variables reported by Kaluzny et al. (2004) that lie within the ACIS-I field of view. The probability that even one of these IDs is due to a chance alignment is only 16%, as the adopted error circles encompass only 0.06% of the ACIS-I field. No additional matches were found to variables in the Weldrake, Sackett & Bridges (2007) catalog.

Next we checked which of these 8 matches are to stars that are likely to be cluster members. Three of the 8 were previously identified with XMM sources by Kaluzny et al. (2004) and found to be non-members on the basis of their proper motions and/or positions in a color-magnitude diagram (see Table 2, bottom section). Of the five remaining identifications, two (NV371=11b and NV390=72e) have measured proper motions and are cluster members (membership probability = 100% according to van Leeuwen et al. 2000). Both are variables of unknown type. The other three (V210=73d, V211=52a, and V216=74d) lie either near the turnoff or on the giant branch and are thus also likely to be members (see Kaluzny et al. 1996, these variables correspond to OGLEGC 15, 16, and 22, respectively). Two of these (V210 and V211) are classified as eclipsing Algol systems with periods of  $\sim 1.5$  and 0.6 days, respectively (Kaluzny et al. 1996). The third (V216) was classified initially as a possible RS CVn star (Kaluzny et al. 1996) and more recently as a long-term variable (Kaluzny et al. 2004). The luminosities of these three sources ( $\sim 2 \times 10^{30} - 1 \times 10^{31} \text{ erg s}^{-1}$ ; see Table 2) are typical of binaries of their class (Makarov 2003), which further supports the conclusion of Kaluzny et al. (1996) that they are cluster members.

Finally, comparing to the HD catalog, we identify *Chandra* sources 92a and 104a with HD 116789 and HD 116663, respectively. HD 116789 is an A0V star with  $V = 8.4$  (Hog et al. 1998); despite being  $\sim 9'$  off-axis, its optical position matches the *Chandra* position to within  $1''$  (see Table 2). This star was also identified by Verbunt & Johnston (2000) as the counterpart of a ROSAT-HRI source. HD 116663 is a B9V star with

$V = 8.7$  (Perryman 1997); its optical position is offset by  $\sim 3''$  from the *Chandra* position. This is still well within the *Chandra* positional uncertainty at  $10'$  off-axis (see §3). Assuming both associations are correct, the A0V and B9V stars have  $f_x/f_V = 7.9 \times 10^{-6}$  and  $4.1 \times 10^{-6}$ , respectively, which are typical of their spectral types (Vaiana et al. 1981); we conclude that both associations are likely. The two stars are in the foreground of  $\omega$  Cen. Using their observed vs. intrinsic B-V colors we estimate the extinction to the A0V and B9V stars to be  $A_V = 0.28$  and 0.53, respectively, where  $A_V = 3.12 \times E(B-V)$ . Assuming  $M_V = +0.6$  for the A0V star and  $M_V = +0.2$  for the B9V star (Lang 1992), we estimate distances of  $\sim 320$  and 390 pc, respectively.

## 6. DISCUSSION

These *Chandra* observations more than double the number of X-ray sources known within  $3 r_c$  ( $\sim 78$ ) of the center of  $\omega$  Cen. A majority of the  $\sim 150$  sources in this region are AGN in the background of the cluster. However, a substantial number, estimated at  $\sim 45\text{--}70$ , are associated with the cluster. About 45% of these are in the core; a similar number lie in an annulus between 1-2 core radii. The remaining  $\sim 10\%$  lie between 2-3  $r_c$ . Very few, if any, cluster members lie beyond 3  $r_c$ , although the ACIS-I coverage outside 3  $r_c$  is incomplete. The optical counterparts identified to date show that these sources comprise at least two broad classes of X-ray-bright binary stars. Of the nine likely cluster members with known optical counterparts (see Table 2), roughly half are probable compact accreting binaries. The X-ray emission of such systems arises from current or past accretion onto the white dwarf or neutron star. The others are optically variable stars that are known or likely to be chromospherically active binaries. X-ray emission from these types of binaries typically results from enhanced chromospheric activity owing to fast spin rates induced by tidal locking.

Further clues to the nature of the X-ray source population in  $\omega$  Cen can be gained from an examination of the cluster's X-ray color-magnitude diagram (CMD; see Fig. 6). Here we plot the 164 *Chandra* sources that have non-zero counts in both the hard and soft bands (see Table 1). In the top panel, round symbols indicate where in the cluster a source lies (large solid dots = core; large open circles = 1-2  $r_c$ ; small open circles = 2-3  $r_c$ ; small dots = outside 3  $r_c$ ). Special symbols have been added to those objects for which there are optical IDs: triangles for CVs, an  $\times$  for the qNS, diamonds for chromospherically active binaries, and squares for non-members. We note that all five optically identified non-members lie outside 3  $r_c$ , while all of the members lie inside 3  $r_c$ . In the bottom panel of Fig. 6 we show 68% confidence intervals computed using the Bayesian Estimation of Hardness Ratios software of Park et al. (2006, ver.07-11-2008) assuming a Jeffrey's noninformative prior distribution. For sources with fewer than 15 counts in either the soft or hard band we use the Gaussian quadrature method to compute the confidence intervals; for brighter sources we use the Gibbs sampler. Here it can be seen that sources with  $X_{med} \gtrsim 30$  have well-defined colors, particularly those near the center of the diagram. Fainter sources, especially those far to the right or left of the plot have more uncertain colors, but general trends (hard vs. soft) can still be discerned.

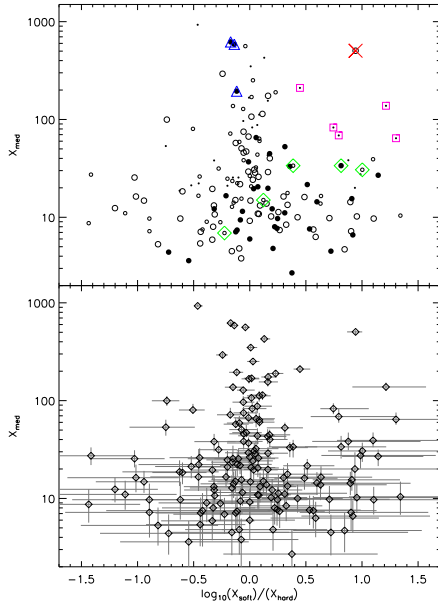


FIG. 6.— X-ray “color-magnitude” diagram for 164 Chandra sources in  $\omega$  Cen with non-zero counts in both hard and soft bands (see Table 1). *Top panel:* Round symbols indicate where in the cluster a source lies (large solid dots = core; large open circles = 1-2  $r_c$ ; small open circles = 2-3  $r_c$ ; dots = outside 3  $r_c$ ). Special symbols indicate optical IDs: triangles for CVs, an  $\times$  for the qNS, diamonds for the chromospherically active binaries, and squares for non-members (see Table 2). *Bottom panel:* 68% confidence intervals computed for sources in the upper panel using the Bayesian method of Park et al. (2006, see §6 for details).

Looking at the confirmed and probable members, we see that among the bright sources, the CVs and qNS have very distinctive colors, with the qNS being very soft and the CVs moderately hard. The fainter sources are active binaries (ABs). They have a large spread in X-ray color, but are softer on average than the CVs. The qNS is quite isolated in the X-ray CMD, as the only object with both the color and luminosity expected for such systems (Rutledge et al. 2002). The CVs, on the other hand, are surrounded by several sources of comparable brightness and color and many fainter sources have similar X-ray colors. Thus it seems likely that at least some of the remaining unidentified sources are CVs. Similarly, the area occupied by the active binaries contains numerous comparable sources. As a first approximation then, we extrapolate the roughly comparable numbers of identified CVs and ABs to the entire population of X-ray sources, and estimate that  $\omega$  Cen contains  $\sim 20$ -35 CVs, and a similar number of active binaries. Given the detection limit of  $L_x \gtrsim 1.2 \times 10^{30}$  erg sec $^{-1}$ , this is likely to represent a large fraction of all the CVs in  $\omega$  Cen, but only a small fraction of chromospherically active binaries, as most such binaries are fainter (Dempsey et al. 1993, 1997).

The radial distribution of X-ray sources in  $\omega$  Cen is consistent with what one would expect for a population of binary stars. Comparing the distribution of X-ray sources (see §4) to the distribution of stars of various mass classes in the model of Meylan (1987) suggests an average mass in the range  $\sim 1.1$ -1.4  $M_\odot$ . This range is reasonable for CVs, active binaries, or a combination of the two.

A constraint can be placed on the number of CVs that could be hiding below the detection limit, as follows. Examining the background rate in the ACIS-I image, we find that it is quite flat out to a radius of at least 7'. In the core, a total of  $\sim 2500$  background counts are present. This implies a  $2\sigma$  upper limit of  $\sim 100$  counts from any faint, unresolved population of sources in the core. The corresponding integrated luminosity is  $L_x = 3 \times 10^{30}$  erg sec $^{-1}$ . For comparison, the faintest known CVs in the Milky Way have  $L_x \sim 5 \times 10^{29}$  erg sec $^{-1}$  (Pretorius 2007). Unless a large fraction of the CV population is exceedingly faint, then the present observations are unlikely to have missed even half.

Several potential CV production mechanisms have been identified since CVs were first observed in globular clusters. Two involve single-single star interactions: tidal capture of a main-sequence (MS) star by a white dwarf (WD), and direct collision of a main-sequence star with a red giant. Given that globular clusters are hosts to non-negligible populations of binary stars, binary+single formation mechanisms must also be considered, such as exchange of a WD into a MS-MS binary (Ivanova et al. 2006). In addition to these dynamical formation mechanisms, CVs may be made directly from primordial binaries, much as they are in the field (Davies 1997). In their recent detailed analysis, Ivanova et al. (2006) find that primordial binaries provide the dominant CV formation channel in model low- and medium-density clusters that span the central density of  $\omega$  Cen.

In considering the primordial channel, we can compare the number of CVs we have inferred in  $\omega$  Cen to the field CV population, which must be primordial. The space density of CVs in the solar neighborhood is  $\sim 10^{-5}$  pc $^{-3}$  (Patterson 1998; Pretorius 2007); given the local mass density of  $\sim 0.1 M_\odot$  pc $^{-3}$ , this translates to  $\sim 10^{-4}$  CVs/ $M_\odot$ . Applying this to  $\omega$  Cen predicts  $\sim 60$  CVs in the core and  $\sim 150$  within the half-mass radius of  $\sim 4.18 = 1.62 r_c$ . Similar estimates are obtained by scaling the prediction of Townsley & Bildsten (2005) for 47 Tuc to  $\omega$  Cen:  $\sim 30$ -80 in the core and  $\sim 70$ -200 within the half-mass radius. Even considering the possibility that as many CVs lie below the detection limit as above it, these predictions are a factor of  $\sim 2$ -3 higher than the number we infer from the present observations. This suggests that at least 1/2 to 2/3 of the primordial binaries that would otherwise give rise to CVs are being destroyed in  $\omega$  Cen before they can evolve to that stage.

A portion of the CVs in  $\omega$  Cen may also be of dynamical origin. Indeed, although their result cannot be taken to apply to any particular individual cluster, Pooley & Hut (2006) have shown that, as a group, CVs in globular clusters are dominated by dynamically formed systems. This finding is based on a sample of 22 GCs—including  $\omega$  Cen—for which deep X-ray imaging with Chandra has been obtained, and applies specifically to relatively X-ray-bright CVs ( $L_x > 4 \times 10^{31}$  erg sec $^{-1}$ ).<sup>8</sup> One hint that at least some of the CVs in  $\omega$  Cen may be of dynamical origin is that the three brightest sources

<sup>8</sup> This limiting  $L_x$  corresponds to  $\sim 100$   $X_{med}$  counts in the present study; 6 sources within the half-mass radius make the color cut imposed by Pooley & Hut (2006) to select probable CVs. Dividing by a cluster mass of  $3 \times 10^5 M_\odot$  yields the specific frequency of 2 per  $10^6 M_\odot$  that they quote.



in the core are all optically identified CVs and all lie within  $0.56 r_c$  of the cluster center (see Fig. 6 and Table 1). Such a distribution, whose chance probability is  $\sim 3\%$ , would naturally result from dynamical formation channels, which favor the creation of CVs with relatively high-mass components that would be most strongly concentrated toward the center of the cluster (and the inner part of the core). High-mass components in turn could help explain their relatively high X-ray luminosities.

Among dynamically formed CVs, the dominant channel in low- to medium-density clusters like  $\omega$  Cen is likely to involve binary+single interactions (Ivanova et al. 2006). No predictions specific to  $\omega$  Cen have yet been made for CVs formed in this way. Meaningful predictions for any given cluster are difficult to make in any case, given continuing uncertainties regarding the size and characteristics of binary populations in GCs. Predictions regarding tidal capture are more straightforward, at least in principle, in that they require knowledge only of the populations of single stars in the cluster. Below we compare our results with two such predictions made specifically for  $\omega$  Cen, both of which made use of multi-mass King-Michie models of  $\omega$  Cen developed by Meylan (1987). We caution that the significance of these comparisons is limited in view of the fact that questions have been raised about the extent to which tidal capture can give rise to stable systems (as opposed to mergers, Podsiadlowski 1996; Mardling 1995).

The first tidal-capture study used the Meylan (1987) models to predict interaction rates among WDs and MS stars of various masses (Verbunt & Meylan 1988). Assuming that tidal capture creates a binary whenever an interaction brings two such stars within 3 stellar radii (without a direct hit), and that CVs have lifetimes of  $10^9$  years, they predicted that  $\omega$  Cen should contain  $\sim 7$  CVs at the present time. They also predicted the radial distribution of CVs; for those with turnoff star MS components (see their Fig. 2a) the distribution is similar to that found here for the X-ray sources in  $\omega$  Cen. A much larger number of tidal-capture CVs was predicted by Di Stefano & Rappaport (1994), who followed the evolution of the binaries produced. With many CVs spending long times at very low mass transfer rates, they predicted  $\sim 90$ -160 CVs, many of which would be quite faint at any given time. These predictions increase to  $\sim 360$ -640 when one considers the full complement of white dwarfs embodied in Meylan's (1987) model of  $\omega$  Cen; Di Stefano & Rappaport (1994) scaled their predictions to 1/4 the number of WDs. Judging from the CV X-ray luminosity function they predict (Di Stefano & Rappaport 1994), the present observations should be sensitive to  $\sim 2/3$  of the total population of CVs. This still leaves the total number of CVs inferred in  $\omega$  Cen an order of magnitude smaller than predicted by Di Stefano & Rappaport (1994), but considerably larger than predicted by Verbunt & Meylan (1988).

Given the many alternate pathways to CVs production in  $\omega$  Cen, and the uncertainties regarding the tidal capture mechanism itself, it is perhaps more interesting to consider how we can use the present observations to place an upper limit on the rate at which tidal capture produces CVs. Davies & Benz (1995) estimate that

$\sim 250$  MS-WD interactions close enough to raise significant tides on the MS star (encounters within  $\sim 3$  stellar radii) have occurred in the core of  $\omega$  Cen over its lifetime. If we assume that about half of the estimated 20-35 CVs are in the core, then even if all of those were the result of tidal capture, only about 5-10% of such close encounters produce a stable binary that is active at the present epoch. If, as suggested by the results of Ivanova et al. (2006), more than 90% of the CVs in a low-to-medium density cluster like  $\omega$  Cen are of primordial and/or binary+single dynamical origin, then this upper limit on the efficacy of tidal capture reduces to less than 1% of all close WD/MS encounters in the cluster.

Finally, we note that radio searches of  $\omega$  Cen have found no millisecond pulsars (MSPs) in the cluster, in stark contrast to 47 Tuc, for example, in which more than a dozen MSPs are known (Grindlay et al. 2002; Heinke et al. 2005). Without speculating about the possible significance of the absence of observed MSPs in  $\omega$  Cen, we note that the present Chandra observations do not rule out the presence of MSPs, as numerous sources occupy the region of the CMD where they would be expected to lie. This is in contrast to the finding by Gendre et al. (2003) who cite the lack of faint sources with soft spectra in the XMM data as further support for the absence of MSPs in  $\omega$  Cen. The X-ray CMD in Fig. 6 can be compared directly to Fig. 3 of Grindlay et al. (2001) for 47 Tuc. In 47 Tuc, 9 MSPs were observed with  $\log(X_{med})=0.8 - 1.5$  and  $X_{color} > 1.0$  (corresponding to  $\log(X_{soft}/X_{hard}) > 0.4$  in our Fig. 6). Adjusting for the somewhat larger hydrogen column to  $\omega$  Cen vs. 47 Tuc (and slightly different distances and exposure times), such MSPs would have  $\log(X_{med}) = 0.7 - 1.4$  in the  $\omega$  Cen CMD; the X-ray colors should not be significantly affected by the slightly increased  $N_H$ . Eighteen objects are found in this range of brightness and color in  $\omega$  Cen (see Fig. 6). Judging from the IDs of brighter objects both within and in front of  $\omega$  Cen (see Table 2 and Fig. 6), this range of colors is also typical of chromspherically active single stars and binaries. Fainter members of these classes undoubtedly populate this region of the CMD and might account for all the observed sources, such that it is possible that none are MSPs. Optical and/or radio identifications will be needed to settle the matter.

## 7. SUMMARY

We have analyzed a 68.6 ksec *Chandra* ACIS-I exposure of the Galactic globular cluster  $\omega$  Cen (NGC 5139). The ACIS-I field of view extends out to nearly twice the half-mass radius, or about three times the core radius. We detect 180 sources to a limiting flux of  $\sim 4.3 \times 10^{-16}$  erg cm $^{-2}$  s $^{-1}$  ( $L_x = 1.2 \times 10^{30}$  erg sec $^{-1}$  at 4.9 kpc). We estimate that 45-70 of the sources are cluster members, most of the remainder being active galactic nuclei. About 45% of the sources are in the core; a similar number lie in an annulus between 1-2 core radii. The remaining  $\sim 10\%$  lie between 2-3  $r_c$ . Very few, if any, cluster members lie beyond 3  $r_c$ , although this is not definitive since the ACIS-I coverage outside 3  $r_c$  is incomplete.

Fourteen of the sources have optical identifications; of these, nine are cluster members. Among the nine cluster members, four are accreting binaries (3 CVs and one quiescent neutron star). The other five are likely to be bi-



nary stars in which one component has an active corona. Extrapolating these optical identifications to the remaining unidentified X-ray source population, we estimate that about 20-35 of the sources are CVs and a similar number are active binaries. This is likely to represent most of the CVs in the cluster, but only a small fraction of all the active binaries. The radial distribution of X-ray sources suggests binary masses in the range 1.1-1.4 $M_{\odot}$ , which is compatible with CVs, active binaries, or a combination of the two.

We place a  $2\sigma$  upper limit of  $L_x < 3 \times 10^{30}$  erg sec $^{-1}$  on the integrated luminosity of any additional faint, unresolved population of sources in the core; unless any remaining CVs are unusually faint, we are unlikely to have missed even half. The total number of CVs per unit mass in  $\omega$  Cen appears to be at least 2-3 times lower than in the field. Thus, even if we posit that all the CVs in  $\omega$  Cen are of primordial origin, some binaries that would otherwise lead to CVs are being destroyed in the cluster. A dynamical origin of at least some of the CVs is not excluded; indeed, the concentration of all the brightest optically-identified CVs in the central part of the cluster core hints at a dynamical origin for at least the brighter systems. We place an upper limit of 5-10% on the fraction of close MS-WD encounters in  $\omega$  Cen that have yielded a stable binary that is active at the present time.

Finally, we note that 166 of the 180 sources found here

have yet to be identified optically. Work is underway to use a mosaic of ACS/WFC images to identify the subset of sources that lie in the inner  $11' \times 11'$  of the ACIS-I field (Cool et al. 2009). Among the unidentified sources are 18 with luminosities and X-ray colors consistent with those of MSPs seen in clusters like 47 Tuc. No MSPs are yet known in  $\omega$  Cen, and it is possible that these X-ray sources are all active binaries and/or objects in the foreground or background. Identifications at other wavelengths are needed for these and other X-ray sources in  $\omega$  Cen to better constrain the numbers and properties of its populations of binary stars and their progeny.

We acknowledge discussions with Jay Anderson, David Pooley, and Craig Heinke. Support for this work was provided by the National Aeronautics and Space Administration through *Chandra* Award Number GO0-1040A issued by the *Chandra* X-ray Observatory Center, which is operated by the Smithsonian Astrophysical Observatory for and on behalf of the National Aeronautics Space Administration under contract NAS8-03060. DH gratefully acknowledges the NASA Harriett G. Jenkins Pre-doctoral Fellowship Program and generous publication support from the University of Washington Astronomy Department's Jacobsen Fund.

## REFERENCES

- Bedin, L. R., Piotto, G., Anderson, J., Cassisi, S., King, I. R., Momany, Y., Carraro, G. 2004, ApJ, 605, 125  
 Carson, J. E., Cool, A. M., & Grindlay, J. E. 2000, ApJ, 532, 461  
 Cool, A. M., *et al.* 2009, in preparation  
 Cool, A. M., Haggard, D., & Carlin, J. L. 2002, in ASP Conf. Ser. 265, Omega Centauri, A Unique Window into Astrophysics, ed. F. van Leeuwen, J. D. Hughes, & G. Piotto San Francisco: ASP 277  
 Cool, A. M., Grindlay, J. E., Bailyn, C. D., Callanan, P. J., & Hertz, P. 1995, ApJ, 438, 719  
 Davies, M. B. 1997, MNRAS, 288, 117  
 Davies, M. B. & Benz, W. 1995, MNRAS, 276, 876  
 Dempsey, R. C., Linsky, J. L., Fleming, T. A., & Schmitt, J. H. M. 1993, ApJS, 86, 599  
 Dempsey, R. C., Linsky, J. L., Fleming, T. A., Schmitt, J. H. M. 1997, ApJ, 478, 358  
 Di Stefano R., & Rappaport, S. 1994, ApJ, 423, 274  
 Feigelson, E. D., Broos, P., Gaffney, J. A., Garmire, G., Hillenbrand, L. A., Pravdo, S. H., Townsley, L., Tsuboi, Y. 2002, ApJ, 574, 258  
 Freeman, P. E., Kashyap, V., Rosner, R., & Lamb, D. Q. 2002, ApJS, 138, 185  
 Fregeau, J. M. 2008, ApJ, 673, 25  
 Fregeau, J. M., Gurkan, M. A., Joshi, K. J., & Rasio, F. A., 2003, ApJ, 593, 772  
 Gendre, B., Barret, D., Webb, N. A. 2003, A&A, 400, 521  
 Giacconi, R., *et al.* 2001, ApJ, 551, 624  
 Gratton, R., Sneden, C., Carretta, E. 2004, ARA&A, 42, 385  
 Grindlay, J. E., Camilo, F., Heinke, C. O., Edmonds, P. D., Cohn, H., Lugger, P. 2002, ApJ, 581, 470  
 Grindlay, J. E., Heinke, C., Edmonds, P. D., Murray, S. S. 2001, Science, 292, 2290  
 Haggard, D., Cool, A. M., Anderson, J., Edmonds, P. D., Callanan, P. J., Heinke, C. O., Grindlay, J. E., Bailyn, C. D. 2004, ApJ, 613, 512  
 Haggard, D., Dorfman, J. L., Cool, A. M., Anderson, J., Bailyn, C. D., Edmonds, P. E., & Grindlay, J. E. 2003, BAAS, 35, 1289  
 Haggard, D., Carlin, J. L., Cool, A. M., Zhao, B., Bailyn, C. D., Edmonds, P. D., Grindlay, J. E., Davies, M. B. 2002a, BAAS, 34, 654  
 Haggard, D., Fuller, A. D., Dorfman, J. L., Cool, A. M., Anderson, J., Edmonds, P. D., Davies, M. B. 2002b, BAAS, 34, 1104  
 Harris, W. E. 1996, AJ, 112, 1487  
 Hartwick, F. D. A., Grindlay, J. E., Cowley, A. P. 1982, ApJ, 254, 11  
 Heinke, C. O., Grindlay, J. E., Edmonds, P. D., Cohn, H. N., Lugger, P. M., Camilo, F., Bogdanov, S., Freire, P. C. 2005, ApJ, 625, 796  
 Hertz, P., & Grindlay, J. E. 1983, ApJ, 275, 105  
 Hog, E., Kuzmin, A., Bastian, U., Fabricius, C., Kuimov, K., Lindgren, L., Makarov, V. V., & Roeser, S. 1998, A&A, 335, 65  
 Ivanova, N., Heinke, C. O., Rasio, F. A., Taam, R. E., Belczynski, K., & Fregeau, J. 2006, MNRAS, 372, 1043  
 Johnston, H. M., Verbunt, F., & Hasinger, G. 1994, A&A, 289, 763  
 Kaluzny, J., Kubiak, M., Szymanski, M., Udalski, A., Krzeminski, W., Mateo, M. 1996, A&AS, 120, 139  
 Kaluzny, J., Olech, A., Thompson, I. B., Pych, W., Krzeminski, W., & Schwarzenberg-Czerny, A. 2004, A&A, 424, 1101  
 Lang, K. R. 1992, Astrophysical Data: Planets and Stars, New York: Springer-Verlag  
 Makarov, V. V. 2003, AJ, 126, 1996  
 Mardling, R. A. 1995, ApJ, 450, 732  
 Margon, B. & Bolte, M. 1987, ApJ, 321, 61  
 McLaughlin, D. E. & Meylan, G. 2003, in ASP Conf. Ser. 296: New Horizons in Globular Cluster Astronomy, ed. G. Piotto, G. Meylan, S. G. Djorgovski & M. Riello San Francisco: ASP 153  
 Meylan, G. 2002, in ASP Conf. Ser. 265: Omega Centauri, A Unique Window into Astrophysics, ed. F. van Leeuwen, J. D. Hughes, & G. Piotto San Francisco: ASP 3  
 Meylan, G. 1987, A&A, 184, 144  
 Okada, Y., Kokubun, M., Takayuki, T., & Makishima, K. 2007, PASJ, 59, 727  
 Park, T., Kashyap, V. L., Siemiginowska, A., van Dyk, D. A., Zezas, A., Heinke, C., & Wargelin, B. J. 2006, ApJ, 652, 610  
 Patterson, J. 1998, PASP, 110, 1132  
 Perryman, M. A. C., *et al.* 1997, A&A, 323, 49

- Piotto, G., Villanova, S., Bedin, L. R., Gratton, R., Cassisi, S., Momany, Y., Recio-Blanco, A., Lucatello, S., Anderson, J., King, I. R., Pietrinferni, A., Carraro, G. 2005, *ApJ*, 621, 777
- Podsiadlowski, P. 1996, *MNRAS*, 279, 1104
- Pooley, D. & Hut, P. 2006, *ApJ*, 646, L143
- Pretorius, M. L., Knigge, C., O'Donoghue, D., Henry, J. P., Gioia, I. M., Mullis, C. R. 2007 *MNRAS*, 382, 1279
- Pryor, C., & Meylan, G. 1993, in *Structure and Dynamics of Globular Clusters*, eds. S. G. Djorgovski & G. Meylan (ASP Conf. Ser. 50), 357
- Rutledge, R. E., Bildsten, L., Brown, E. F., Pavlov, G. G., & Zavlin, V. E. 2002, *ApJ*, 578, 405
- Townsley, L. K., & Bildsten, L. 2005 *ApJ*, 628, 395
- Townsley, L. K., Broos, P. S., Garmire, G. P., Nousek, J. A. 2000 *ApJ*, 534, 139
- Tozzi et al. 2001, *ApJ*, 562, 42
- Trager, S. C., King, I. R., & Djorgovski, S. 1995, *AJ*, 109, 218
- Vaiana, G. S. et al. 1981, *ApJ*, 244, 163
- van Leeuwen, F., Le Poole, R. S., Reijns, R. A., Freeman, K. C., & de Zeeuw, P. T. 2000, *A&A*, 360, 472
- Verbunt, F., & Johnston, H. M. 2000, *A&A*, 358, 910
- Verbunt, F., & Meylan, G. 1988, *A&A*, 203, 297
- Weldrake, D. T. F., Sackett, P. D., & Bridges, T. J. 2007, *AJ*, 133, 1447

TABLE 1  
 $\omega$  CEN X-RAY SOURCES

Src <sup>a</sup>	Position CXOHCD <sup>b</sup>	Offset ( $r_c$ )	Detected Counts/Corrected Counts					$\frac{X_{\text{soft}}}{X_{\text{hard}}}$	$f_x$ (erg cm <sup>-2</sup> s <sup>-1</sup> )	Previous X-ray ID <sup>d</sup>	Optical ID <sup>e</sup>
			$X_{\text{med}}$	$X_{\text{soft}}$	$X_{\text{hard}}$	$X_{\text{CDF5}}$					
11a	J132641.59-472832.1	0.28	3/2.7	2/1.9	1/0.8	3/2.9	2.5	2.9 x 10 <sup>-16</sup>	...	...	
11b	J132641.03-472737.8	0.50	14/33.7	12/29.3	2/4.5	13/31.7	6.5	3.6 x 10 <sup>-15</sup>	XMM24	NV371	
11c	J132643.91-472720.8	0.51	8/8.0	5/5.0	3/3.0	6/6.1	1.7	8.5 x 10 <sup>-16</sup>	...	...	
12a	J132648.66-472744.9	0.38	182/194.9	85/91.0	107/119.0	128/137.1	0.8	2.1 x 10 <sup>-14</sup>	HRI20,ACIS18	CV1	
12b	J132652.54-472738.0	0.58	26/65.3	14/35.3	12/31.0	25/63.1	1.1	6.9 x 10 <sup>-15</sup>	XMM61	...	
13a	J132653.51-472900.4	0.52	627/621.3	282/279.4	394/413.5	421/417.2	0.7	6.6 x 10 <sup>-14</sup>	HRI9a,ACIS6,XMM5	CV2	
13b	J132650.57-472918.2	0.41	20/19.8	12/11.9	8/8.2	16/15.9	1.5	2.1 x 10 <sup>-15</sup>	...	...	
13c	J132652.14-472935.6	0.56	594/587.9	276/273.1	362/375.3	399/394.9	0.7	6.3 x 10 <sup>-14</sup>	HRI9b,ACIS4,XMM2	CV3	
13d	J132649.56-472924.9	0.39	13/12.2	8/7.6	5/4.8	10/9.5	1.6	1.3 x 10 <sup>-15</sup>	...	...	
13e	J132646.28-472948.7	0.47	5/11.7	5/11.8	0/0	5/11.8	-	1.2 x 10 <sup>-15</sup>	...	...	
13f	J132645.99-472916.5	0.26	11/11.1	8/8.2	4/4.0	9/9.2	2.0	1.2 x 10 <sup>-15</sup>	...	...	
14a	J132645.74-472858.9	0.14	5/4.8	3/2.9	2/1.8	4/3.9	1.6	5.1 x 10 <sup>-16</sup>	...	...	
14b	J132645.01-472852.4	0.12	5/4.4	1/0.7	4/3.7	3/2.7	0.2	4.7 x 10 <sup>-16</sup>	...	...	
14c	J132644.09-472856.9	0.18	27/26.9	25/25.1	2/1.8	27/27.1	14.1	2.9 x 10 <sup>-15</sup>	XMM92	...	
14d	J132637.99-472910.9	0.56	12/11.5	7/6.8	8/7.9	9/8.7	0.9	1.2 x 10 <sup>-15</sup>	XMM101	...	
21a	J132631.20-472827.8	0.96	21/20.5	12/11.8	10/10.0	17/16.7	1.2	2.2 x 10 <sup>-15</sup>	...	...	
21b	J132635.34-472759.2	0.73	6/5.7	6/6.0	0/0	6/5.9	-	6.1 x 10 <sup>-16</sup>	...	...	
21c	J132636.87-472746.1	0.68	6/6.0	3/3.0	3/3.0	5/5.1	1.0	6.4 x 10 <sup>-16</sup>	...	...	
21d	J132638.26-472740.5	0.62	21/21.6	16/16.6	5/5.1	20/20.8	3.3	2.3 x 10 <sup>-15</sup>	...	...	
21e	J132645.20-472652.7	0.67	14/14.4	11/11.5	3/2.9	13/13.5	3.9	1.5 x 10 <sup>-15</sup>	XMM103	...	
22a	J132648.30-472641.2	0.76	5/4.5	4/3.7	1/0.7	5/4.6	5.5	4.8 x 10 <sup>-16</sup>	...	...	
22b	J132649.40-472713.7	0.58	8/7.4	4/3.7	5/4.8	6/5.6	0.8	7.9 x 10 <sup>-16</sup>	...	...	
22c	J132652.67-472713.5	0.70	30/52.7	21/37.0	10/18.0	23/40.5	2.1	5.6 x 10 <sup>-15</sup>	XMM44	...	
22d	J132658.75-472729.0	0.95	16/15.5	14/13.8	2/1.7	15/14.7	8.1	1.6 x 10 <sup>-15</sup>	...	...	
22e	J132659.93-472809.7	0.94	33/33.1	23/23.2	10/10.2	29/29.3	2.3	3.5 x 10 <sup>-15</sup>	...	...	
22f	J132658.84-472821.2	0.85	19/19.6	10/10.4	9/9.6	13/13.5	1.1	2.1 x 10 <sup>-15</sup>	...	...	
23a	J132651.05-473010.2	0.69	37/36.9	19/19.0	19/19.5	28/28.0	1.0	3.9 x 10 <sup>-15</sup>	...	...	
23b	J132651.71-473047.4	0.93	10/9.7	7/6.9	4/3.9	10/9.9	1.8	1.0 x 10 <sup>-15</sup>	...	...	
23c	J132648.07-473014.6	0.65	12/12.2	4/4.0	8/8.3	8/8.1	0.5	1.3 x 10 <sup>-15</sup>	...	...	
24a	J132644.46-473006.0	0.58	7/7.1	3/3.0	4/4.0	6/6.2	0.8	7.5 x 10 <sup>-16</sup>	...	...	
24b	J132639.22-473037.5	0.89	5/4.8	5/5.1	0/0	5/5.0	-	5.1 x 10 <sup>-16</sup>	...	...	
24c	J132638.42-473036.8	0.92	17/16.6	8/7.8	13/12.7	10/9.8	0.6	1.8 x 10 <sup>-15</sup>	...	...	
24d	J132637.44-473007.4	0.81	8/7.6	6/5.8	2/1.7	7/6.7	3.5	8.1 x 10 <sup>-16</sup>	...	...	
24e	J132636.79-473011.6	0.85	3/2.6	3/2.9	0/0	3/2.8	-	2.8 x 10 <sup>-16</sup>	...	...	
24f	J132637.26-472942.7	0.71	7/6.6	6/5.8	1/0.7	7/6.7	8.6	7.0 x 10 <sup>-16</sup>	...	...	
24g	J132634.39-472955.8	0.91	44/44.7	27/27.5	18/18.3	34/34.6	1.5	4.8 x 10 <sup>-15</sup>	XMM72	...	
24h	J132637.67-472918.6	0.60	10/9.4	5/4.7	6/5.7	6/5.6	0.8	1.0 x 10 <sup>-15</sup>	...	...	
31a	J132629.38-472813.3	1.09	28/29.3	16/16.8	16/17.3	20/21.0	1.0	3.1 x 10 <sup>-15</sup>	XMM50	...	
31b	J132631.37-472801.5	0.98	8/7.7	5/4.9	3/2.8	5/4.8	1.7	8.2 x 10 <sup>-16</sup>	...	...	
31c	J132632.31-472708.4	1.06	9/13.2	5/7.4	4/6.0	7/10.5	1.2	1.4 x 10 <sup>-15</sup>	...	...	
31d	J132636.23-472622.2	1.07	39/40.1	25/25.8	16/17.1	32/33.0	1.5	4.3 x 10 <sup>-15</sup>	...	...	
32a	J132646.34-472518.6	1.28	11/10.8	6/5.9	5/4.9	9/8.9	1.2	1.1 x 10 <sup>-15</sup>	...	...	
32b	J132652.11-472533.0	1.25	7/7.1	2/1.9	5/5.2	2/1.9	0.4	7.5 x 10 <sup>-16</sup>	...	...	
32c	J132655.88-472602.3	1.19	5/9.7	1/1.9	4/7.9	2/3.9	0.2	1.0 x 10 <sup>-15</sup>	...	...	
32d	J132702.40-472647.0	1.29	10/9.7	9/8.9	1/0.7	9/8.9	12.5	1.0 x 10 <sup>-15</sup>	...	...	
32e	J132703.05-472725.4	1.21	5/4.7	5/4.9	0/0	5/4.9	-	5.0 x 10 <sup>-16</sup>	...	...	
32f	J132705.33-472808.8	1.29	16/16.3	12/12.4	6/6.2	15/15.5	2.0	1.7 x 10 <sup>-15</sup>	...	...	
33a	J132701.52-472840.3	1.02	6/5.9	2/1.9	4/4.1	4/4.0	0.5	6.3 x 10 <sup>-16</sup>	...	...	
33b	J132706.52-472853.5	1.36	12/12.4	1/0.9	13/14.3	5/5.1	0.1	1.3 x 10 <sup>-15</sup>	...	...	
33c	J132703.60-472858.2	1.17	7/7.2	6/6.4	1/0.8	7/7.5	8.0	7.7 x 10 <sup>-16</sup>	...	...	
33d	J132701.43-472924.8	1.06	19/19.5	7/7.1	14/15.3	11/11.3	0.5	2.1 x 10 <sup>-15</sup>	...	...	
33e	J132700.92-473004.6	1.14	10/10.9	6/6.6	5/5.6	8/8.9	1.2	1.2 x 10 <sup>-15</sup>	...	...	
33f	J132659.28-473038.0	1.18	9/9.2	5/5.2	5/5.2	7/7.2	1.0	9.8 x 10 <sup>-16</sup>	...	...	
33g	J132656.03-473046.0	1.07	6/5.4	6/5.7	0/0	6/5.6	-	5.7 x 10 <sup>-16</sup>	...	...	
33h	J132655.08-473113.7	1.18	59/57.5	27/26.3	35/35.1	41/40.0	0.7	6.1 x 10 <sup>-15</sup>	ACIS26,XMM38	...	
33i	J132651.08-473144.8	1.26	75/75.0	36/36.0	40/40.9	50/50.0	0.9	8.0 x 10 <sup>-15</sup>	ACIS29,XMM36	...	
33j	J132649.56-473124.5	1.11	9/8.4	6/5.7	3/2.7	8/7.6	2.1	8.9 x 10 <sup>-16</sup>	...	...	
33k	J132649.80-473147.9	1.26	24/24.2	13/13.1	12/12.3	16/16.2	1.1	2.6 x 10 <sup>-15</sup>	XMM35	...	
33l	J132648.73-473125.3	1.10	105/106.8	56/57.0	53/55.1	71/72.3	1.0	1.1 x 10 <sup>-14</sup>	HRI21,ACIS23,XMM9	...	
33m	J132646.47-473141.2	1.19	10/10.2	6/6.2	4/4.0	7/7.2	1.5	1.1 x 10 <sup>-15</sup>	XMM108	...	
34a	J132639.51-473125.4	1.17	5/4.7	5/4.9	1/0.7	5/4.9	7.0	5.0 x 10 <sup>-16</sup>	...	...	
34b	J132637.42-473053.0	1.04	116/114.0	67/65.9	52/50.8	91/89.5	1.3	1.2 x 10 <sup>-14</sup>	ACIS17,XMM20	...	
34c	J132635.53-473029.4	0.99	4/3.6	1/0.8	3/2.8	2/1.8	0.3	3.8 x 10 <sup>-16</sup>	...	...	
34d	J132634.33-473033.5	1.07	64/66.8	34/35.5	35/36.4	47/49.1	1.0	7.1 x 10 <sup>-15</sup>	ACIS25,XMM60	...	
41a	J132624.41-472657.8	1.55	15/15.0	7/7.0	9/9.4	10/10.1	0.7	1.6 x 10 <sup>-15</sup>	...	...	
41b	J132626.59-472634.6	1.49	5/11.3	3/7.2	2/4.0	4/9.5	1.8	1.2 x 10 <sup>-15</sup>	...	...	
41c	J132624.52-472611.3	1.69	10/16.3	1/1.5	9/15.5	4/6.5	0.1	1.7 x 10 <sup>-15</sup>	...	...	
41d	J132628.66-472627.4	1.40	72/99.7	15/20.5	76/112.4	35/48.7	0.2	1.1 x 10 <sup>-14</sup>	XMM49	...	

TABLE 1 — *Continued*

Src <sup>a</sup>	Position CXOHCD <sup>b</sup>	Offset ( $r_c$ )	Detected Counts/Corrected Counts				$X_{\text{soft}}/X_{\text{hard}}$	$f_x$ ( $\text{erg cm}^{-2} \text{s}^{-1}$ )	Previous X-ray ID <sup>d</sup>	Optical ID <sup>e</sup>
			$X_{\text{med}}$	$X_{\text{soft}}$	$X_{\text{hard}}$	$X_{\text{CDFs}}^c$				
41e	J132630.55–472602.3	1.42	10/9.8	8/8.2	2/1.6	10/10.2	5.0	$1.0 \times 10^{-15}$	XMM80	...
41f	J132632.05–472451.5	1.71	29/30.7	17/18.1	15/16.5	23/24.5	1.1	$3.3 \times 10^{-15}$	...	...
41g	J132637.41–472429.9	1.69	28/28.6	16/16.5	14/14.8	23/23.7	1.1	$3.0 \times 10^{-15}$	XMM126	...
41h	J132643.89–472442.8	1.52	6/5.5	0/0	7/7.1	2/1.6	–	$5.8 \times 10^{-16}$	...	...
42a	J132701.56–472543.8	1.52	11/10.7	4/3.8	8/7.8	5/4.8	0.5	$1.1 \times 10^{-15}$	...	...
42b	J132707.58–472601.8	1.74	10/10.0	7/7.2	3/2.7	8/8.2	2.7	$1.1 \times 10^{-15}$	...	...
42c	J132709.63–472729.4	1.61	6/5.4	2/1.7	5/4.7	3/2.6	0.4	$5.7 \times 10^{-16}$	...	...
43a	J132707.96–472945.4	1.51	10/14.8	5/7.5	5/7.4	9/13.7	1.0	$1.6 \times 10^{-15}$	...	...
43b	J132706.19–473004.9	1.45	8/7.5	6/5.9	2/1.6	6/5.8	3.7	$8.0 \times 10^{-16}$	...	...
43c	J132706.90–473009.6	1.50	8/7.4	5/4.8	3/2.6	8/7.8	1.8	$7.9 \times 10^{-16}$	...	...
43d	J132704.52–473038.0	1.45	22/21.8	11/10.9	13/13.3	16/15.9	0.8	$2.3 \times 10^{-15}$	XMM127	...
43e	J132703.43–473056.3	1.46	7/6.3	6/5.8	2/1.5	7/6.7	3.8	$6.7 \times 10^{-16}$	...	...
43f	J132656.03–473202.2	1.48	14/14.3	12/12.6	2/1.6	12/12.5	7.9	$1.5 \times 10^{-15}$	...	...
43g	J132651.52–473202.6	1.38	6/5.3	1/0.7	5/4.6	2/1.6	0.1	$5.6 \times 10^{-16}$	...	...
43h	J132649.57–473212.7	1.42	50/50.6	24/24.3	28/28.8	36/36.5	0.8	$5.4 \times 10^{-15}$	ACIS33,XMM57	...
44a	J132644.12–473231.5	1.52	161/174.6	96/104.2	66/71.6	128/139.0	1.5	$1.9 \times 10^{-14}$	ACIS13,XMM16	...
44b	J132633.50–473153.7	1.51	15/14.8	2/1.7	15/14.9	4/3.7	0.1	$1.6 \times 10^{-15}$	...	...
44c	J132623.64–473044.1	1.67	14/13.4	9/8.9	5/4.1	10/9.8	2.2	$1.4 \times 10^{-15}$	XMM117	...
44d	J132622.87–473009.4	1.62	26/25.9	15/15.2	13/12.7	18/18.2	1.2	$2.8 \times 10^{-15}$	...	...
44e	J132619.80–472910.7	1.72	450/504.7	405/455.2	46/51.9	442/496.5	8.8	$5.4 \times 10^{-14}$	HRI7,ACIS3,XMM4	qNS
51a	J132631.29–472439.7	1.81	45/47.0	23/24.2	24/26.0	35/36.9	0.9	$5.0 \times 10^{-15}$	XMM59	...
51b	J132630.76–472347.2	2.12	9/8.7	1/0.4	10/10.9	4/3.7	0.04	$9.3 \times 10^{-16}$	...	...
51c	J132639.51–472340.3	1.96	9/8.0	3/2.5	6/5.3	7/6.6	0.5	$8.5 \times 10^{-16}$	...	...
51d	J132641.00–472402.3	1.80	29/29.0	17/17.3	12/11.9	24/24.5	1.5	$3.1 \times 10^{-15}$	XMM67	...
51e	J132644.71–472333.7	1.96	11/10.2	9/9.0	2/1.0	11/11.0	9.5	$1.1 \times 10^{-15}$	...	...
52a	J132647.35–472316.5	2.07	8/6.9	3/2.5	5/4.2	6/5.5	0.6	$7.3 \times 10^{-16}$	...	V211
52b	J132654.91–472409.2	1.83	5/4.5	2/1.8	3/2.6	3/2.7	0.7	$4.8 \times 10^{-16}$	...	...
52c	J132706.38–472538.2	1.77	43/45.8	21/22.4	24/25.4	30/32.0	0.9	$4.9 \times 10^{-15}$	ACIS40,XMM82	...
52d	J132714.91–472743.8	1.93	14/13.2	5/4.6	10/9.6	8/7.6	0.5	$1.4 \times 10^{-15}$	...	...
52e	J132717.01–472819.6	2.04	10/8.9	4/3.5	7/6.4	4/3.3	0.6	$9.5 \times 10^{-16}$	XMM102	...
52f	J132714.57–472830.8	1.88	17/16.1	13/12.9	5/4.2	15/14.8	3.1	$1.7 \times 10^{-15}$	XMM47	...
53a	J132659.79–473235.8	1.79	15/13.8	9/8.6	7/6.1	13/12.5	1.4	$1.5 \times 10^{-15}$	...	...
53b	J132647.01–473400.0	2.09	4/1.4	2/0.9	2/0	2/0.6	–	$1.5 \times 10^{-16}$	...	...
54a	J132643.98–473335.1	1.93	6/4.7	5/4.6	1/0	6/5.4	–	$5.0 \times 10^{-16}$	...	...
54b	J132642.44–473309.2	1.77	26/25.5	3/2.5	27/26.6	12/11.7	0.1	$2.7 \times 10^{-15}$	...	...
54c	J132627.03–473215.4	1.88	18/18.4	5/4.9	19/19.5	9/9.1	0.3	$2.0 \times 10^{-15}$	...	...
54d	J132625.14–473227.4	2.02	155/169.6	84/92.2	84/88.9	111/122.0	1.0	$1.8 \times 10^{-14}$	HRI10,ACIS15,XMM8	...
54e	J132625.41–473140.8	1.79	5/3.8	3/2.6	4/3.1	5/4.5	0.8	$4.0 \times 10^{-16}$	...	...
54f	J132621.87–473050.3	1.79	10/9.0	9/8.9	1/0	10/9.8	–	$9.6 \times 10^{-16}$	...	...
54g	J132620.03–473015.4	1.81	6/4.8	3/2.5	4/3.1	4/3.4	0.8	$5.1 \times 10^{-16}$	...	...
54h	J132620.37–473003.1	1.76	277/293.3	111/117.5	192/205.4	179/189.7	0.6	$3.1 \times 10^{-14}$	ACIS10,XMM13	...
61a	J132620.83–472450.1	2.20	8/5.8	1/0	7/5.6	5/3.9	–	$6.2 \times 10^{-16}$	...	...
61b	J132641.52–472216.6	2.47	128/137.3	57/61.2	80/86.4	83/89.4	0.7	$1.5 \times 10^{-14}$	ACIS19,XMM15	...
62a	J132648.50–472218.9	2.45	11/9.0	4/3.1	9/7.5	6/5.0	0.4	$9.6 \times 10^{-16}$	XMM77	...
62b	J132708.00–472333.9	2.43	57/59.0	27/28.1	35/34.8	42/44.1	0.8	$6.3 \times 10^{-15}$	ACIS34,XMM41	...
62c	J132712.32–472424.5	2.38	22/20.7	11/10.6	12/10.3	13/12.4	1.0	$2.2 \times 10^{-15}$	XMM110	...
62d	J132716.28–472459.1	2.44	15/13.2	13/12.7	2/0	13/12.4	–	$1.4 \times 10^{-15}$	...	...
62e	J132724.16–472820.4	2.51	18/16.5	14/13.8	5/3.2	14/13.5	4.3	$1.8 \times 10^{-15}$	...	...
63a	J132723.00–472907.8	2.44	26/24.8	11/10.5	17/16.6	17/16.6	0.6	$2.6 \times 10^{-15}$	...	...
63b	J132714.65–473150.6	2.26	25/23.5	12/11.4	17/16.3	17/16.4	0.7	$2.5 \times 10^{-15}$	XMM114	...
63c	J132711.77–473240.7	2.31	238/251.6	133/141.0	122/132.1	178/188.8	1.1	$2.7 \times 10^{-14}$	ACIS11,XMM11	...
63d	J132710.00–473320.2	2.42	78/80.2	21/21.1	64/67.7	37/37.9	0.3	$8.5 \times 10^{-15}$	ACIS35,XMM34	...
63e	J132702.09–473355.5	2.32	13/11.0	2/0.9	13/11.6	3/1.7	0.1	$1.2 \times 10^{-15}$	...	...
63f	J132657.01–473351.3	2.16	13/10.8	12/11.4	1/0	12/11.1	–	$1.1 \times 10^{-15}$	...	...
63g	J132656.75–473428.1	2.38	15/14.1	6/5.6	9/7.8	7/6.4	0.7	$1.5 \times 10^{-15}$	...	...
64a	J132627.01–473409.1	2.48	71/71.7	31/31.4	48/46.8	48/49.0	0.7	$7.6 \times 10^{-15}$	ACIS37,XMM40	...
64b	J132624.44–473303.0	2.22	27/27.3	2/1.0	26/26.0	13/13.0	0.04	$2.9 \times 10^{-15}$	...	...
64c	J132616.29–473058.8	2.14	26/26.5	13/13.5	14/13.5	16/16.6	1.0	$2.8 \times 10^{-15}$	...	...
64d	J132614.08–473020.6	2.19	16/12.8	7/5.0	9/7.2	10/7.5	0.7	$1.4 \times 10^{-15}$	...	...
71a	J132604.26–472806.1	2.73	16/7.5	7/2.2	10/5.8	10/3.9	0.4	$8.0 \times 10^{-16}$	...	...
71b	J132604.60–472741.3	2.73	38/32.3	23/20.2	20/17.8	29/25.3	1.1	$3.4 \times 10^{-15}$	XMM76	...
71c	J132612.76–472413.3	2.76	61/63.6	34/36.1	28/29.7	48/51.2	1.2	$6.8 \times 10^{-15}$	ACIS39,XMM79	...
71d	J132617.43–472337.6	2.69	13/9.7	3/1.3	12/10.2	6/4.0	0.1	$1.0 \times 10^{-15}$	...	...
71e	J132623.13–472251.1	2.69	37/38.3	19/20.1	22/22.8	26/27.7	0.9	$4.1 \times 10^{-15}$	XMM39	...
72a	J132648.28–472149.4	2.64	17/13.8	12/11.1	6/2.6	14/12.7	4.2	$1.5 \times 10^{-15}$	...	...
72b	J132654.52–472204.8	2.59	518/562.3	257/279.3	287/305.8	370/402.4	0.9	$6.0 \times 10^{-14}$	ACIS5,XMM32	...
72c	J132716.07–472359.0	2.67	18/15.5	8/7.0	11/8.3	14/13.2	0.8	$1.6 \times 10^{-15}$	...	...
72d	J132723.44–472446.5	2.88	33/31.5	13/12.3	25/23.3	19/18.3	0.5	$3.3 \times 10^{-15}$	...	...

TABLE 1 — *Continued*

Src <sup>a</sup>	Position CXOHCD <sup>b</sup>	Offset ( $r_c$ )	Detected Counts/Corrected Counts				$X_{\text{CDFS}}^c$	$\frac{X_{\text{soft}}}{X_{\text{hard}}}$	$f_x$ ( $\text{erg cm}^{-2} \text{s}^{-1}$ )	Previous X-ray ID <sup>d</sup>	Optical ID <sup>e</sup>
			$X_{\text{med}}$	$X_{\text{soft}}$	$X_{\text{hard}}$						
72e	J132724.38–472512.2	2.85	18/15.0	9/7.8	9/5.9	11/9.4	1.3	$1.6 \times 10^{-15}$	...	NV390	
72f	J132725.00–472715.6	2.61	11/7.2	3/1.2	12/9.4	6/3.9	0.1	$7.7 \times 10^{-16}$	...	...	
73a	J132721.71–473206.2	2.71	39/39.2	34/36.4	6/2.9	35/36.9	12.5	$4.2 \times 10^{-15}$	XMM74	...	
73b	J132721.00–473234.5	2.76	20/17.7	12/11.5	8/5.3	16/15.4	2.2	$1.9 \times 10^{-15}$	...	...	
73c	J132659.29–473458.2	2.62	61/60.3	34/34.2	30/28.0	41/41.1	1.2	$6.4 \times 10^{-15}$	ACIS38,XMM52	...	
73d	J132647.33–473600.8	2.87	32/30.6	27/29.2	8/2.9	31/33.2	10.2	$3.3 \times 10^{-15}$	...	V210	
74a	J132628.95–473437.0	2.58	14/10.4	12/11.0	4/0.5	12/10.4	23.6	$1.1 \times 10^{-15}$	...	...	
74b	J132627.57–473456.4	2.73	122/128.1	59/62.2	70/71.2	88/93.2	0.9	$1.4 \times 10^{-14}$	ACIS22,XMM30	...	
74c	J132617.24–473408.7	2.85	20/14.7	3/0.1	20/15.8	4/0.5	0.008	$1.6 \times 10^{-15}$	...	...	
74d	J132608.22–473032.7	2.58	37/33.7	25/24.1	13/9.9	31/29.7	2.4	$3.6 \times 10^{-15}$	...	V216	
74e	J132606.00–4721919.6	2.63	50/43.7	29/24.8	23/21.2	36/31.1	1.2	$4.6 \times 10^{-15}$	XMM51	...	
74f	J132604.93–472901.5	2.69	32/22.3	17/10.6	17/13.7	22/14.5	0.8	$2.4 \times 10^{-15}$	...	...	
81a	J132634.96–472052.2	3.08	31/27.5	26/26.2	8/2.7	27/26.6	9.6	$2.9 \times 10^{-15}$	XMM73	...	
82a	J132706.92–472133.0	3.06	17/17.6	2/0	18/19.8	6/4.4	–	$1.9 \times 10^{-15}$	...	...	
82b	J132710.03–472127.8	3.19	57/64.3	50/60.3	8/3.0	54/64.5	19.8	$6.8 \times 10^{-15}$	XMM68	NV377	
82c	J132717.88–472256.3	3.04	23/18.7	6/3.6	19/15.2	10/7.4	0.2	$2.0 \times 10^{-15}$	...	...	
82d	J132721.14–472324.1	3.07	93/96.5	43/44.9	52/51.3	68/72.1	0.9	$1.0 \times 10^{-14}$	HRI19,ACIS27,XMM18	...	
82e	J132728.28–472423.0	3.23	77/82.9	41/45.0	42/42.8	52/57.2	1.1	$8.8 \times 10^{-15}$	ACIS32,XMM94	...	
82f	J132729.30–472554.1	3.03	394/427.9	235/256.5	177/190.7	305/333.1	1.3	$4.5 \times 10^{-14}$	HRI6,ACIS7,XMM6	...	
82g	J132730.65–472655.0	3.01	30/25.5	13/11.1	18/14.0	16/13.7	0.8	$2.7 \times 10^{-15}$	...	...	
83a	J132727.44–473132.8	2.95	181/189.6	117/124.2	68/73.1	147/156.1	1.7	$2.0 \times 10^{-14}$	ACIS14,XMM12	...	
83b	J132720.13–473335.0	2.96	22/16.6	7/4.5	17/12.9	13/10.3	0.3	$1.8 \times 10^{-15}$	...	...	
83c	J132722.91–473359.0	3.19	46/43.1	26/25.4	21/17.6	34/33.4	1.4	$4.6 \times 10^{-15}$	...	...	
83d	J132718.50–473405.1	3.01	26/21.2	8/5.6	22/18.6	10/7.1	0.3	$2.3 \times 10^{-15}$	...	...	
83e	J132712.87–473456.9	3.02	327/349.4	176/188.9	174/185.4	240/257.9	1.0	$3.7 \times 10^{-14}$	ACIS8,XMM23	...	
84a	J132639.15–473631.3	3.10	84/87.8	45/49.8	46/42.7	56/62.3	1.2	$9.3 \times 10^{-15}$	ACIS30,XMM45	...	
84b	J132638.05–473634.3	3.13	18/25.5	8/10.9	12/15.4	9/11.8	0.7	$2.7 \times 10^{-15}$	...	...	
84c	J132613.70–473440.7	3.16	88/112.0	49/65.5	46/54.0	64/84.5	1.2	$1.2 \times 10^{-14}$	ACIS28,XMM22	...	
84d	J132611.52–473403.1	3.08	195/210.3	143/156.5	56/55.9	175/191.5	2.8	$2.2 \times 10^{-14}$	ACIS12,XMM25	V167	
84e	J132605.04–473151.5	2.96	30/26.1	9/6.9	23/19.3	17/15.1	0.4	$2.8 \times 10^{-15}$	...	...	
84f	J132600.78–472912.3	2.96	39/21.1	30/21.1	10/0	33/20.4	–	$2.2 \times 10^{-15}$	XMM62	...	
91a	J132619.02–472105.9	3.40	30/21.0	13/9.8	23/15.5	18/13.3	0.6	$2.2 \times 10^{-15}$	...	...	
91b	J132638.49–472001.2	3.37	84/82.8	65/69.5	21/12.5	73/76.4	5.6	$8.8 \times 10^{-15}$	ACIS31,XMM31	NV378	
92a	J132646.24–471946.1	3.43	129/138.0	117/132.5	17/8.1	120/133.7	16.4	$1.5 \times 10^{-14}$	HRI18,ACIS21,XMM28	HD 116789	
92b	J132707.82–472035.0	3.43	44/38.3	33/34.0	14/4.5	39/38.8	7.5	$4.1 \times 10^{-15}$	...	...	
92c	J132736.31–472553.2	3.47	15/3.5	6/1.7	10/0	8/1.7	–	$3.7 \times 10^{-16}$	...	...	
93a	J132739.62–473024.3	3.59	18/22.2	6/7.4	16/21.1	9/11.1	0.3	$2.4 \times 10^{-15}$	XMM84	...	
93b	J132734.02–473235.9	3.51	22/20.0	12/17.3	12/2.0	17/24.5	8.8	$2.1 \times 10^{-15}$	...	...	
93c	J132700.29–473715.3	3.48	46/38.1	17/13.9	36/28.9	28/24.0	0.5	$4.1 \times 10^{-15}$	XMM113	...	
94a	J132601.59–473305.8	3.38	819/930.0	227/256.3	657/746.2	446/506.4	0.3	$9.9 \times 10^{-14}$	PSPC11,ACIS2,XMM1	...	
94b	J132557.25–473249.5	3.58	149/155.4	88/95.2	70/65.7	114/123.6	1.5	$1.7 \times 10^{-14}$	ACIS20,XMM21	...	
101a	J132623.54–471924.8	3.86	161/167.1	81/85.4	88/86.8	115/122.8	1.0	$1.8 \times 10^{-14}$	ACIS24,XMM17	...	
102a	J132743.43–472810.4	3.77	65/53.5	17/9.5	58/53.2	30/22.1	0.2	$5.7 \times 10^{-15}$	...	...	
104a	J132549.07–473127.3	3.88	73/68.7	53/57.1	23/9.2	59/61.8	6.2	$7.3 \times 10^{-15}$	...	HD 116663	

NOTE. — <sup>a</sup>Source ID assigned in this work. <sup>b</sup>Registered acronym – for details see Dictionary of Nomenclature of Celestial Objects (<http://vizier.u-strasbg.fr/viz-bin/Dic>). Source positions have the format JHHMMSS.ss+DDMMSS.s. <sup>c</sup>X-ray counts in the *Chandra* Deep Field South soft X-ray band (0.5 – 2.0 keV). <sup>d</sup>Previous X-ray ID References: [PSPC] Johnston, Verbunt & Hasinger 1994; [HRI] Verbunt & Johnston 2000; [ACIS] Rutledge *et al.* 2002; [XMM] Gendre *et al.* 2003. <sup>e</sup>Optical ID References: [HD] Hog *et al.* 1998, Perryman *et al.* 1997; [CV] Carson, Cool, & Grindlay 2000, Haggard *et al.* (2002b, 2003); [qNS] Haggard *et al.* 2004; [V,NV] Kaluzny *et al.* 2004.

TABLE 2  
OPTICAL IDENTIFICATIONS

Source	Optical ID	Optical Position (J2000)		Raw Offsets <sup>a</sup> (")		Corr. Offsets <sup>b</sup> (")		Apparent <sup>c</sup> Mag	$L_x^d$ ( <i>erg s</i> <sup>-1</sup> )	Var <sup>e</sup> Type
		R.A.	Dec.	$\Delta\alpha$ , $\Delta\delta$	$\Delta\alpha$ , $\Delta\delta$					
<b>Members</b>										
11b	NV371	13 26 41.09	-47 27 37.4	0.6, 0.4	0.1, -0.1	15.9	$1.0 \times 10^{31}$	unkn		
12a	CV1	13 26 48.66	-47 27 44.6	0.0, 0.3	0.0, 0.0	21.1	$6.0 \times 10^{31}$	CV		
13a	CV2	13 26 53.51	-47 29 00.1	0.0, 0.3	0.0, 0.0	19.6	$1.9 \times 10^{32}$	CV		
13c	CV3	13 26 52.13	-47 29 35.3	-0.1, 0.3	-0.1, 0.0	20.2	$1.8 \times 10^{32}$	CV		
44e	qNS	13 26 19.81	-47 29 10.3	0.2, 0.3	0.2, 0.0	25.2	$1.6 \times 10^{32}$	qNS		
52a	V211	13 26 47.38	-47 23 15.7	0.6, 0.5	0.1, 0.0	18.1	$2.1 \times 10^{30}$	EA		
72e	NV390	13 27 24.45	-47 25 11.8	0.7, 0.4	0.2, -0.1	14.1	$4.6 \times 10^{30}$	unkn		
73d	V210	13 26 47.34	-47 35 59.9	0.2, 0.7	-0.3, 0.2	16.9	$9.5 \times 10^{30}$	EA		
74d	V216	13 26 08.24	-47 30 32.5	0.3, 0.5	-0.2, 0.0	15.1	$1.0 \times 10^{31}$	LT		
<b>Non-members</b>										
82b	NV377	13 27 10.10	-47 21 27.4	0.7, 0.4	0.2, -0.1	15.8	...	irr		
84d	V167	13 26 11.56	-47 34 02.8	0.4, 0.3	-0.1, -0.2	—	...	irr		
91b	NV378	13 26 38.53	-47 19 59.5	0.4, 1.7	-0.1, 1.2	14.7	...	EA		
92a	HD 116789	13 26 46.33	-47 19 46.1	0.9, 0.0	0.9, 0.0	8.4	$1.7 \times 10^{29}$	A0V		
104a	HD 116663	13 25 49.00	-47 31 30.3	-0.7, -3.0	-0.7, -3.0	8.7	$1.4 \times 10^{29}$	B9V		

NOTE. — <sup>a</sup>Offsets are calculated as optical position minus X-ray position; <sup>b</sup>Besite corrections of (0'0, 0'3) and (0'5, 0'5) have been applied to the HST and Kaluzny *et al.* (2004) counterparts, respectively (see §5); <sup>c</sup>Apparent magnitudes are given in the following bands: (1) 13c, 13a, and 12a — HST WFPC2 R<sub>675</sub> (Carson, Cool & Grindlay 2000); (2) 44e — HST ACS R<sub>625</sub> (Haggard *et al.* 2004); (3) 73d and 52a — V-band at maximum light (Kaluzny *et al.* 2004); (4) 74d — Average of the 1993 and 1994 V-band maxima (Kaluzny *et al.* 1996); (5) 92a — V-band (Hog *et al.* 1998); (6) 104a — V-band (Perryman *et al.* 1997). <sup>d</sup>X-ray luminosities for cluster members are calculated using a distance of 4.9kpc; for foreground stars HD 116789 and HD 116663, distances of 320 and 390 pc were used (see §5). <sup>e</sup>CV: Cataclysmic Variable; qNS: transient neutron star in quiescence; EA: Eclipsing Algol-type binary; LT: long-term irregular or long-period variable; irr: irregular light curve; unkn: unknown variable type.